

# Improved Performance of High-Entropy Disordered Rocksalt Oxyfluoride Cathode by Atomic Layer Deposition Coating for Li-Ion Batteries

Bei Zhou, Siyu An, David Kitsche, Sören L. Dreyer, Kai Wang, Xiaohui Huang, Jannik Thanner, Matteo Bianchini, Torsten Brezesinski, Ben Breitung, Horst Hahn, and Qingsong Wang\*

Lithium-excess cation-disordered rocksalt materials are a promising class of transition metal-based cathodes that exhibit high specific capacity and energy density. The exceptional performance is achieved through participation of anionic redox in addition to cationic redox reactions in the electrochemistry. However, anionic redox reactions accompanied by oxygen evolution, accelerated electrolyte breakdown, and structural evolution lead to voltage hysteresis and low initial Coulombic efficiency. Herein, an  $\text{Al}_2\text{O}_3$  layer with varying thickness has been coated onto a high-entropy disordered rocksalt oxyfluoride cathode through atomic layer deposition to enhance battery performance. The results indicate that the utilization of a uniform  $\text{Al}_2\text{O}_3$  coating improves the capacity retention and rate capability of the cathode, with the performance being strongly dependent on the layer thickness. Further investigation into cathode–electrolyte interfacial reactions reveals that the thin protecting  $\text{Al}_2\text{O}_3$  coating can reduce the decomposition of electrolyte on the cathode surface but cannot prevent bulk phase degradation during prolonged cycling. These findings highlight the need for optimized coating design on the disordered rocksalt cathode to improve battery performance.

of lithium and transition metals (TMs) in the same sublattice, display superior structural stability and facile diffusion of  $\text{Li}^+$ . The electrochemical activity of the DRX structure is enabled by lithium transport through a percolating O-TM network (tetrahedral sites with no face-sharing TM ions).<sup>[5]</sup> Significant efforts have been devoted to achieving improved electrochemical performance of DRX cathodes. Many DRX cathodes have previously demonstrated high specific capacities of  $q_{\text{dis}} > 200 \text{ mA h g}^{-1}$  associated with combined cationic (TM) and anionic (Oxygen) redox reactions.<sup>[6,7]</sup> Considering the local coordination in DRX, the Li–O–Li configuration results in nonbonding O  $2p$  states with high energy, which can be more easily oxidized, thereby triggering oxygen redox.<sup>[8]</sup> Recently, Lun et al. have synthesized and characterized a series of high-entropy oxyfluoride DRX compounds,


## 1. Introduction

With the growing demand of high-performance lithium-ion batteries, a series of Li-excess cathode materials, including layered and cation-disordered rocksalt (DRX) oxides, have been developed.<sup>[1–4]</sup> DRX cathodes, featuring a random distribution

confirming the participation of reversible oxygen oxidation and reduction processes in the electrochemistry.<sup>[9]</sup> In the reported high-entropy compound  $\text{Li}_{1.3}\text{Mn}^{\text{II}}_{0.1}\text{Co}_{0.1}\text{Mn}^{\text{III}}_{0.1}\text{Cr}_{0.1}\text{Ti}_{0.1}\text{Nb}_{0.2}\text{O}_{1.7}\text{F}_{0.3}$ , with the initial discharge capacity of  $307 \text{ mA h g}^{-1}$ ,  $\text{Co}^{2+}/\text{Co}^{3+}$ ,  $\text{Mn}^{2+}/\text{Mn}^{4+}$  and  $\text{Cr}^{3+}/\text{Cr}^{6+}$  are utilized as TM redox couples which could contribute to the total TM redox capacity of  $222.9 \text{ mA h g}^{-1}$ .

B. Zhou, S. An, D. Kitsche, S. L. Dreyer, K. Wang, X. Huang, T. Brezesinski, B. Breitung, H. Hahn  
Institute of Nanotechnology  
Karlsruhe Institute of Technology (KIT)  
Kaiserstr. 12, 76131 Karlsruhe, Germany

B. Zhou, H. Hahn  
KIT-TUD Joint Laboratory Nanomaterials  
Technische Universität Darmstadt  
Otto-Berndt-Str. 3, 64206 Darmstadt, Germany

 The ORCID identification number(s) for the author(s) of this article can be found under <https://doi.org/10.1002/ssstr.202400005>.

© 2024 The Authors. Small Structures published by Wiley-VCH GmbH. This is an open access article under the terms of the Creative Commons Attribution License, which permits use, distribution and reproduction in any medium, provided the original work is properly cited.

DOI: 10.1002/ssstr.202400005

B. Zhou, M. Bianchini, Q. Wang  
Bavarian Center for Battery Technology (BayBatt)  
Universität Bayreuth  
Weiherstr. 26, 95448 Bayreuth, Germany  
E-mail: qingsong.wang@uni-bayreuth.de

J. Thanner, M. Bianchini, Q. Wang  
Department of Chemistry  
Universität Bayreuth  
Universitätsstr. 30, 95447 Bayreuth, Germany

H. Hahn  
School of Sustainable Chemical  
Biological and Materials Engineering  
University of Oklahoma  
201 Stephenson Pkwy., Norman, OK 73019, USA

They also demonstrated that the high-entropy strategy can suppress short-range order, facilitating lithium transport. As disordered and multicomponent systems, high-entropy cathodes with rich chemical diversity provide more possibilities for adjusting the charge compensation behavior.<sup>[10,11]</sup> Nevertheless, in the charging process, the highly oxidized oxygen species are inevitably involved in side reactions between electrode and electrolyte, accompanied by irreversible oxygen loss and large voltage hysteresis.<sup>[12,13]</sup> Furthermore, reaction of hydrogen fluoride (HF) with the cathode surface and decomposition of liquid electrolyte at the surface cause degradation.<sup>[14]</sup>

Surface modification, i.e., electrochemically inert coatings as protective films [or artificial cathode–electrolyte interphase (CEI)], can largely suppress the side reactions between electrode and organic electrolyte, especially at high potentials when the cathode becomes more oxidizing.<sup>[15,16]</sup> In the last few decades, atomic layer deposition (ALD) has been developed and considered as a promising coating strategy for precisely controlling the coating thickness on the atomic scale to sustain desirable conductivity for effective battery performance, despite coating with electronically or ionically insulating materials.<sup>[17–20]</sup> There are many reports on coating of cathode materials via ALD, including  $\text{LiNi}_{0.4}\text{Mn}_{0.4}\text{Co}_{0.2}\text{O}_2$ ,  $\text{LiMn}_2\text{O}_4$ , and  $\text{Li}_{1.2}\text{Ti}_{0.4}\text{Mn}_{0.4}\text{O}_2$ .<sup>[21–23]</sup> Conformal coating has been demonstrated to effectively protect cathode materials, thereby increasing the Coulombic efficiency (reversibility) in the initial cycle, among others.<sup>[24]</sup> Specifically for the deposition of  $\text{Al}_2\text{O}_3$  conformal thin films, the metal-organic precursor trimethylaluminum (TMA) and  $\text{H}_2\text{O}$  as coreactant offer the advantages of low cost and ease of deposition.<sup>[25]</sup> However, few studies have focused on the structural retention of bulk materials and the chemical stability of ALD coatings, both of which is important for cathode optimization.

In this work, ALD-assisted  $\text{Al}_2\text{O}_3$  coatings of different thickness were deposited onto a high-entropy oxyfluoride DRX cathode material,  $\text{Li}_{1.3}\text{Mn}^{\text{II}}_{0.1}\text{Co}_{0.1}\text{Mn}^{\text{III}}_{0.1}\text{Cr}_{0.1}\text{Ti}_{0.1}\text{Nb}_{0.2}\text{O}_{1.7}\text{F}_{0.3}$  (in the following referred to as TM6), to increase the surface stability during cycling. As known for state-of-the-art cathode materials, improved stability can promote lithium diffusion kinetics and helps suppress interfacial side reactions. The modified high-entropy DRX cathode was indeed found to exhibit improved initial Coulombic efficiency, capacity retention, rate capability, and reduced polarization compared to the pristine counterpart. Additionally, galvanostatic intermittent titration technique

(GITT) and electrochemical impedance spectroscopy (EIS) measurements were performed to study the lithium diffusion kinetics. Furthermore, differential electrochemical mass spectrometry (DEMS) was used to examine the gassing behavior, while the parasitic reactions occurring at the interface between electrode and electrolyte and the bulk structural evolution during cycling were probed using X-ray photoelectron spectroscopy (XPS) and X-ray diffraction (XRD), respectively.

## 2. Results and Discussion

### 2.1. Structure and Morphology

Figure 1 shows XRD patterns of the pristine TM6 and  $\text{TM6-10Al}_2\text{O}_3$  ( $\text{TM6-nAl}_2\text{O}_3$ ,  $n$  indicates the number of ALD cycles in the coating process) powder samples, which can be indexed as a phase-pure rocksalt structure (space group  $Fm-3m$ ). Diffraction peaks for  $\text{Al}_2\text{O}_3$  could not be observed because of its presumably amorphous state and/or the low coating content. The lattice parameter decreased slightly after  $\text{Al}_2\text{O}_3$  coating, which may be attributed to trace amounts of  $\text{Al}^{3+}$  entering the rocksalt lattice during the heating in the ALD reaction chamber because the ionic radius of  $\text{Al}^{3+}$  (0.535 Å) is smaller than that of  $\text{Li}^+$  (0.76 Å),  $\text{Mn}^{3+}$  (0.645 Å, high spin), and  $\text{Ti}^{4+}$  (0.605 Å). Note that  $\text{Li}^+$  might also diffuse into the  $\text{Al}_2\text{O}_3$  layer and therefore lead to some lithium deficiency in the DRX cathode, resulting in a decreased lattice parameter. Further decrease in lattice parameter of the samples is observed with increasing coating thickness, as demonstrated in Figure S1, Supporting Information. The lattice parameter change is also consistent with the tendency reported previously.<sup>[26]</sup> The results from Rietveld refinement are given in Table S1–S3, Supporting Information.

To confirm the successful deposition of  $\text{Al}_2\text{O}_3$  onto the surface of the TM6 cathode, the as-prepared samples were characterized by XPS. As shown in Figure 2a, both TM6 and  $\text{TM6-10Al}_2\text{O}_3$  produce peaks characteristic of Co, Mn, Cr, Ti, and Nb. The Al 2p spectra are presented in Figure 2b, and a peak at a binding energy of 74.6 eV is only observed for  $\text{TM6-10Al}_2\text{O}_3$ , which represents the Al–O chemical bonding of  $\text{Al}_2\text{O}_3$  on the coated material.<sup>[27]</sup> In Figure 2c, the O 1s spectrum is fitted into two components at 529.7 and 531.8 eV, which can be attributed to TM–O in DRX or Al–O in  $\text{Al}_2\text{O}_3$  and the presence of  $\text{Li}_2\text{CO}_3$  on the surface of both samples, respectively.<sup>[28,29]</sup> The TM–O peak is more intense after

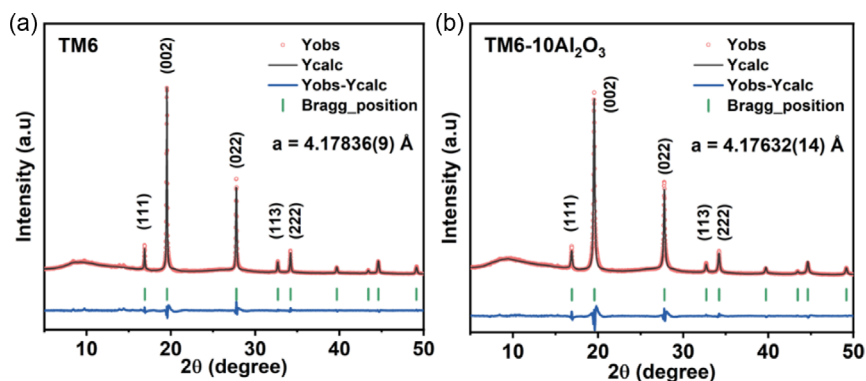
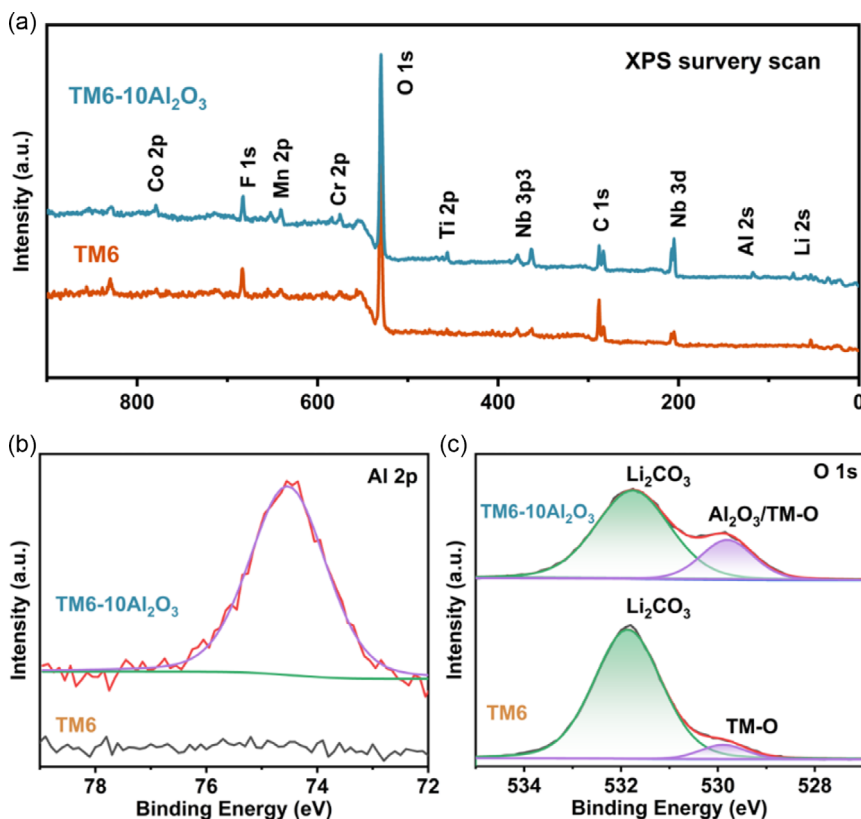


Figure 1. a,b) XRD patterns of TM6 and  $\text{TM6-10Al}_2\text{O}_3$  ( $\lambda = 0.70932$  Å).



**Figure 2.** a) XPS survey and b) detail spectra of the Al 2p and c) O 1s regions of TM6 and TM6-10Al<sub>2</sub>O<sub>3</sub>.

coating, confirming that the TM6 particle surface is successfully covered with an Al<sub>2</sub>O<sub>3</sub> layer.

Scanning electron microscopy (SEM) analysis revealed that the TM6-10Al<sub>2</sub>O<sub>3</sub> sample consists of nanoparticle aggregates varying in size from 1 to 10 μm (Figure 3a). The transmission electron microscopy (TEM) image and corresponding selected-area electron diffraction (SAED) pattern in Figure 3b,c display the morphology of the particle and indicate the polycrystalline nature of the rocksalt material. To further investigate the distribution of the different elements in the bulk material and the uniformity of the surface coating, elemental mapping using scanning TEM–energy-dispersive X-ray spectroscopy (STEM–EDX) was performed. The uniform distribution of all elements on the nanometer scale could be confirmed (Figure 3d). In addition, the EDX line profile scanned along the edge of the coated material demonstrates the homogeneity of the Al<sub>2</sub>O<sub>3</sub> coating with a few nanometers in thickness on the surface of the particles.

## 2.2. Electrochemical Performance

The electrochemical performance of uncoated and Al<sub>2</sub>O<sub>3</sub>-coated materials was evaluated via galvanostatic cycling between 1.5 and 4.8 V at a current rate of 0.1C. The initial charge–discharge profiles are shown in Figure 4a for the TM6 and TM6-10Al<sub>2</sub>O<sub>3</sub> cathodes. The low-voltage sloping region corresponds to TM oxidation. A flatter profile can be observed at high potentials,

originating from the oxygen oxidation beyond the theoretical TM redox charging compensation limit. This has been proven by Lun et al. through detecting the characteristic oxygen feature at an excitation energy of ≈531 eV using O K-edge resonant inelastic X-ray scattering.<sup>[30]</sup> In principle, with proceeding delithiation, the contribution of lattice oxygen oxidation to the overall capacity increases.<sup>[31,32]</sup> The initial specific discharge capacities for pristine TM6 and TM6-10Al<sub>2</sub>O<sub>3</sub> were 255 and 275 mA h g<sup>-1</sup>, with initial Coulombic efficiency values of 68.6 and 85.4%, respectively. Note that the initial specific capacity of TM6 did not reach that of the reported TM6 (with the initial discharge capacity of 307 mA h g<sup>-1</sup> at 20 mA g<sup>-1</sup> in the voltage range of 1.5–4.7 V) by Lun et al.<sup>[9]</sup> This might be due to the lower reaction kinetics of TM6 in this work, attributed to the larger particle size, which was limited by the ball-milling conditions during electrode processing.<sup>[33]</sup> As demonstrated in a previous report, the anionic redox reactions at high potentials are believed to result in oxygen evolution, especially in the initial cycle, causing low Coulombic efficiency.<sup>[17]</sup> Therefore, a higher initial discharge capacity and Coulombic efficiency of TM6-10Al<sub>2</sub>O<sub>3</sub> can be ascribed to increased reversible oxygen activity and suppression of interfacial side reactions between cathode and electrolyte. Moreover, for the uncoated TM6 cathode, the initial charge and discharge curves show a large voltage hysteresis, which is always associated with TM migration and O<sub>2</sub> formation.<sup>[12]</sup> By comparison, for TM6-10Al<sub>2</sub>O<sub>3</sub>, the mitigation of voltage hysteresis in the first and 30th cycle can be observed (Figure 4a,b). The uncoated TM6 sample also displays severe voltage fade upon cycling,

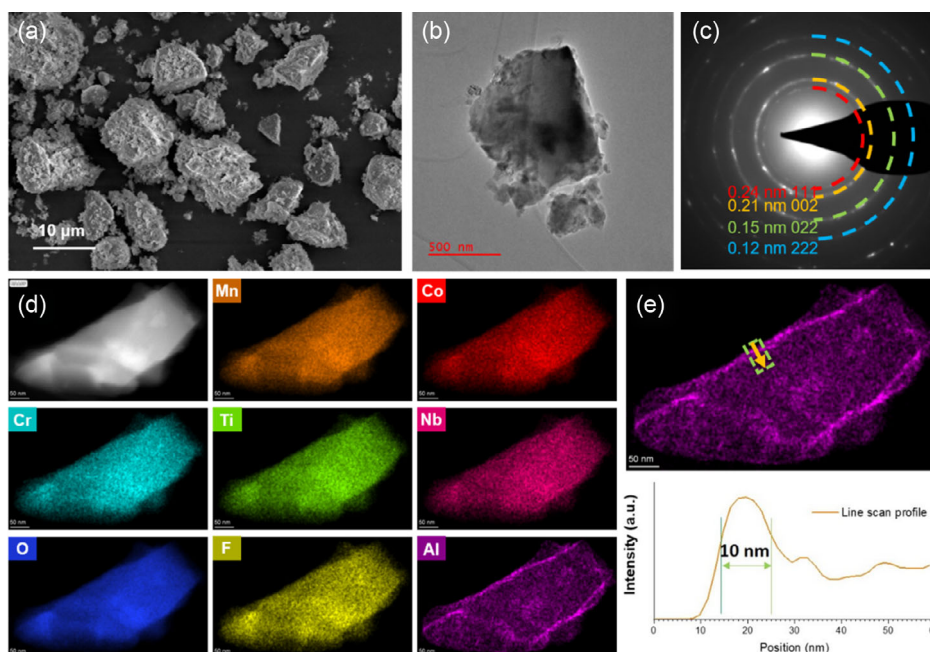


**Figure 3.** Electron microscopy characterization of TM6-10Al<sub>2</sub>O<sub>3</sub>: a) SEM image, b) TEM image, c) SAED pattern, and d) STEM-EDX mapping. e) Line scan profile revealing the thickness of the Al<sub>2</sub>O<sub>3</sub> coating. The scale bar in (d), (e) is 50 nm.

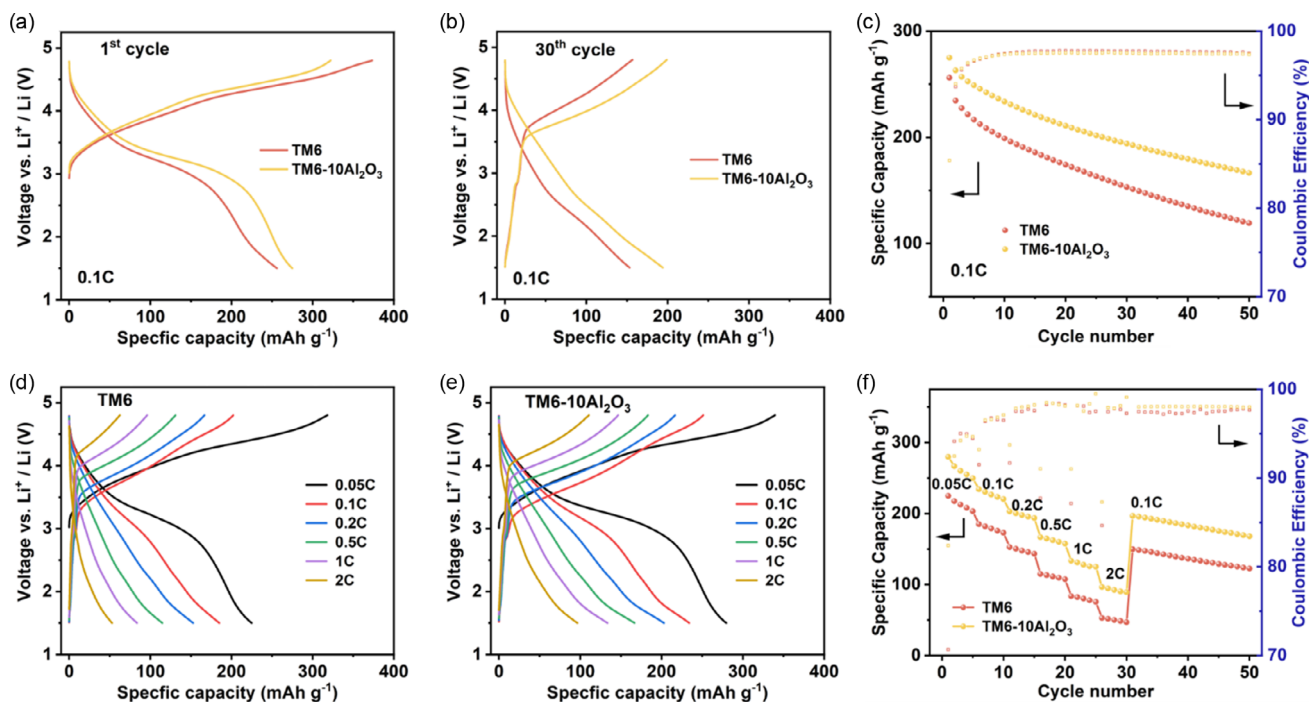


**Figure 4.** Electrochemical performance of TM6 and TM6-10Al<sub>2</sub>O<sub>3</sub> half-cells tested in a potential range of 1.5–4.8 V versus Li<sup>+</sup>/Li: a) initial galvanostatic charge–discharge curves, b) 30th cycle voltage profiles, and c) cycling performance at 0.1C rate. Charge and discharge curves of d) TM6 and e) TM6-10Al<sub>2</sub>O<sub>3</sub> at different C-rates. f) Rate capability and Coulombic efficiency of the cathodes between 0.05 and 2C.

In comparison, the voltage fade is reduced during cycling after Al<sub>2</sub>O<sub>3</sub> coating. However, decreased discharge capacity and greater voltage polarization are observed with a thicker Al<sub>2</sub>O<sub>3</sub> coating (see Figure S2a,b, Supporting Information). This can

be attributed to the insulating nature of the Al<sub>2</sub>O<sub>3</sub> coating. Comparable results were also reported by Huang et al. who investigated the electrochemical properties of Li<sub>1.2</sub>Ti<sub>0.4</sub>Mn<sub>0.4</sub>O<sub>2</sub> with different thickness of an Al<sub>2</sub>O<sub>3</sub> coating.<sup>[22]</sup>

The cycling performance of Li half-cells containing uncoated TM6 and TM6- $n\text{Al}_2\text{O}_3$  samples is shown in Figure 4c and S2c, Supporting Information. The capacity retention for TM6 with 0, 10, 20 and 50  $\text{Al}_2\text{O}_3$  coating cycles after 50 cycles was 46.6%, 60.5%, 61.5%, and 57.4%, respectively. The improved electrochemical performance results from the protective  $\text{Al}_2\text{O}_3$  surface layer, which helps prevent side reactions between active material and electrolyte. This will be further proven in the following XPS analysis. These results indicate that the specific capacity and cycling stability of TM6 have been effectively improved by proper  $\text{Al}_2\text{O}_3$  coating. Based on these results, the TM6-10 $\text{Al}_2\text{O}_3$  sample with superior cyclability was chosen for further characterization.

To investigate the rate capability of the TM6 and TM6-10 $\text{Al}_2\text{O}_3$  cathodes, the cells were charged and discharged galvanostatically between 1.5 and 4.8 V at different C-rates ranging from 0.05 to 2C. The results are shown in Figure 4d–f. The rate performance of the TM6-10 $\text{Al}_2\text{O}_3$  was better than that of TM6. The enhanced rate performance indicates that the  $\text{Al}_2\text{O}_3$  coating can effectively

improve both ionic and electronic partial conductivities of the TM6 cathode. This is further confirmed by EIS, as discussed in the subsequent section. When the C-rate was returned to 0.1C after cycling at higher rates, the retained specific capacity of TM6-10 $\text{Al}_2\text{O}_3$  is  $196.6 \text{ mA h g}^{-1}$ , with the same fading tendency as before. However, the TM6 and TM6-10 $\text{Al}_2\text{O}_3$  cathodes show similar degradation behavior (Figure 4c,f), which indicates that the coating only plays a limited role in increasing conductivity of the particles and does not prevent structural degradation, which starts from the surface to the bulk originating from oxygen loss in DRX materials.<sup>[34]</sup>

Cyclic voltammetric (CV) measurements of TM6 and TM6-10 $\text{Al}_2\text{O}_3$  were conducted at a scan rate of  $0.1 \text{ mV s}^{-1}$  between 1.5 and 4.8 V for 10 cycles. As depicted in Figure 5a,b, the overall features of the profiles are essentially the same. During the first oxidation, two broad peaks located at 3.8 and 4.4 V are observed, roughly corresponding to the occurrence of the TM and oxygen oxidation, respectively.<sup>[35]</sup>  $\text{Co}^{2+}/\text{Co}^{3+}$ ,  $\text{Mn}^{2+}/\text{Mn}^{4+}$ , and  $\text{Cr}^{3+}/\text{Cr}^{6+}$

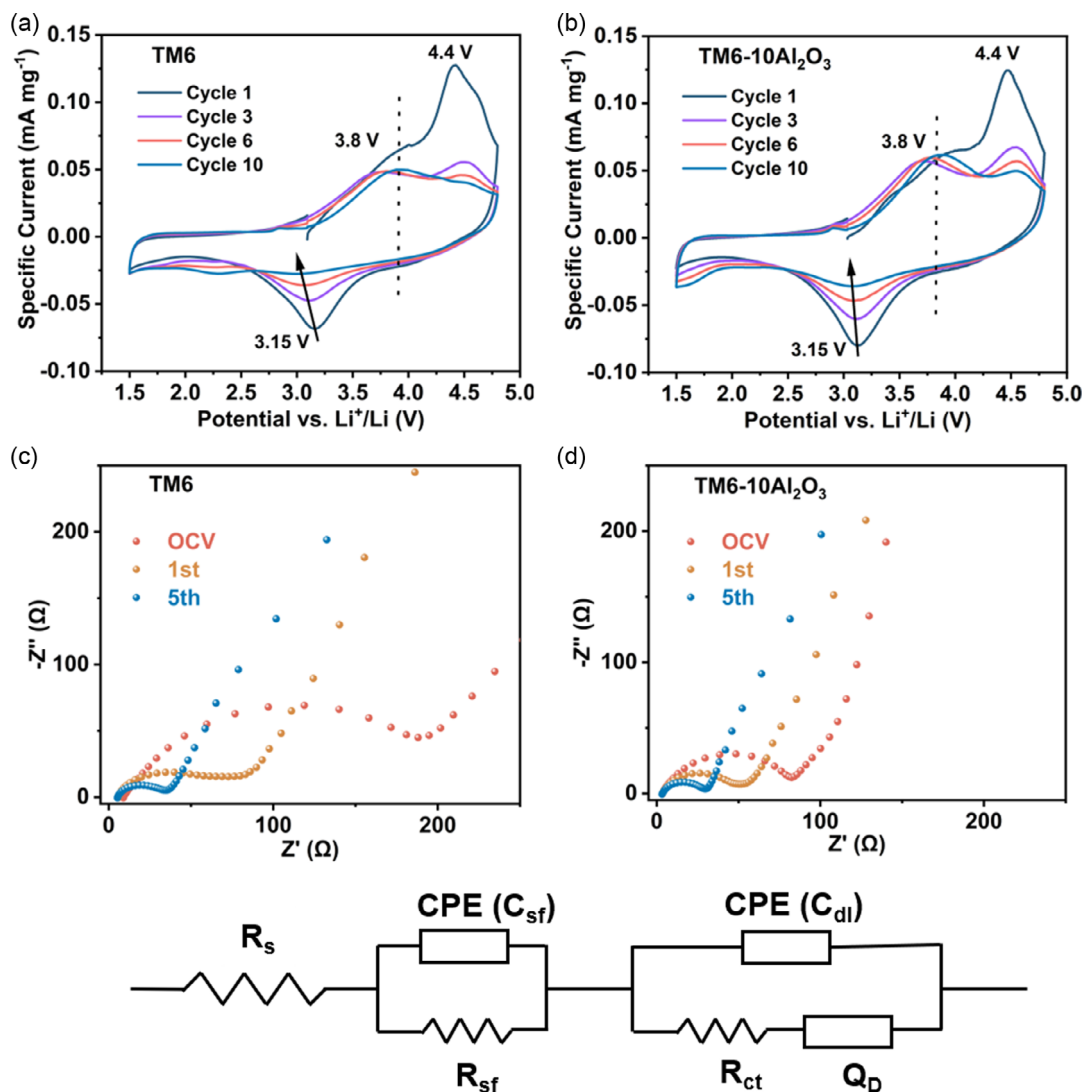


**Figure 5.** CV curves for a) TM6 and b) TM6-10 $\text{Al}_2\text{O}_3$ . Nyquist plots of the electrochemical impedance for c) TM6 and d) TM6-10 $\text{Al}_2\text{O}_3$  after different cycles. The equivalent circuit is shown below the Nyquist plots.

are utilized as TM redox couples as demonstrated by Lun et al. using X-ray absorption spectroscopy.<sup>[30]</sup> In the following cycles, the TM oxidation peak maintains its voltage and current values while the  $O^{2-}/O^{n-}$  oxidation peak current reduces significantly. This is consistent with the high activity but irreversible nature of oxygen oxidation in DRX materials, in sharp contrast to the reversible behavior of the TM redox process. The irreversible oxygen redox leads to the formation of a metal-densified surface layer, which hinders lithium transport. This can explain the decrease in capacity after the initial cycle (specific discharge capacity of  $234.5 \text{ mA h g}^{-1}$  in the second cycle).<sup>[36]</sup> In the first reduction process, a strong TM peak is observed at 3.15 V. For the TM6 cathode, the current of the TM reduction peak gradually decreases while an additional peak at lower potentials gradually increases with extended cycling, indicating that the TM species are reduced to lower valence states.<sup>[37]</sup> In comparison, the shape and current of the oxidation peak in the high-potential range of the TM6-10Al<sub>2</sub>O<sub>3</sub> cathode are better maintained. During the reduction process, the shift of the TM peaks over cycling is negligible. Moreover, the smaller potential difference (indicated by the dashed line in Figure 5a,b) in the oxidation and reduction peaks of the TM6-10Al<sub>2</sub>O<sub>3</sub> cathode demonstrates a lower degree of polarization. This suggests that Al<sub>2</sub>O<sub>3</sub> coating can improve the reversibility of oxygen redox reactions while preserving TM redox activity.

To understand the intrinsic factor of the improvement in the electrochemical performance, EIS measurements were conducted on the TM6 and TM6-10Al<sub>2</sub>O<sub>3</sub> cells before and after cycling. The Nyquist plots and an equivalent circuit are displayed in Figure 5c,d. In the equivalent circuit,  $R_s$  is the ohmic resistance. The semicircle at high frequency can be ascribed to the surface film impedance,  $R_{sf}$ . The compressed semicircle in the high to medium frequency range is assigned to the charge-transfer resistance ( $R_{ct}$ ), and  $C_{dl}$  is the double-layer capacitance. Herein, the constant phase element has been introduced instead of pure capacitive elements  $C_{sf}$  and  $C_{dl}$ . For TM6 and TM6-10Al<sub>2</sub>O<sub>3</sub>, it is likely that two semicircles merged into a larger semicircle. The tail observed in the low-frequency region cannot be modeled properly by a finite Warburg impedance ( $Z_w$ ). This phenomenon can be related to the non-negligible ion diffusion in the electrolyte, the inhomogeneous thickness of the cathodes, or the capacitive reactance of the Li metal counter electrode.<sup>[38,39]</sup> Therefore, a finite diffusion constant phase element (CPE,  $Q_D$ ) is introduced to replace  $Z_w$ .<sup>[40]</sup> It is noted that the value of  $R_s$  is negligible for both samples, indicating small ohmic polarization. Moreover, the Al<sub>2</sub>O<sub>3</sub> coating decreases the diameter of the semicircle in the initial state, demonstrating that the surface layer enhances the charge-transfer kinetics and reduces the passivation film resistance.<sup>[41]</sup> Typically, Al<sub>2</sub>O<sub>3</sub> possesses low electronic conductivity (on the order of  $10^{-8} \text{ S cm}^{-1}$ ). However, Al<sub>2</sub>O<sub>3</sub> can react with the Li<sub>2</sub>CO<sub>3</sub>/LiOH byproduct on the material surface, partially forming LiAlO<sub>2</sub> with high Li-ion conductivity ( $3 \times 10^{-5} \text{ S cm}^{-1}$ ).<sup>[42]</sup> Therefore, the mutual diffusion of surface Al and Li in TM6-10Al<sub>2</sub>O<sub>3</sub> possibly leads to the formation of Li<sub>x</sub>AlO<sub>y</sub> on the surface and thus promotes Li<sup>+</sup> migration.<sup>[43]</sup> The charge-transfer resistance of both cathode materials decreased gradually with increased cycle number. This can be attributed to the enhanced penetration of electrolyte into the electrode after crack formation and formation of a

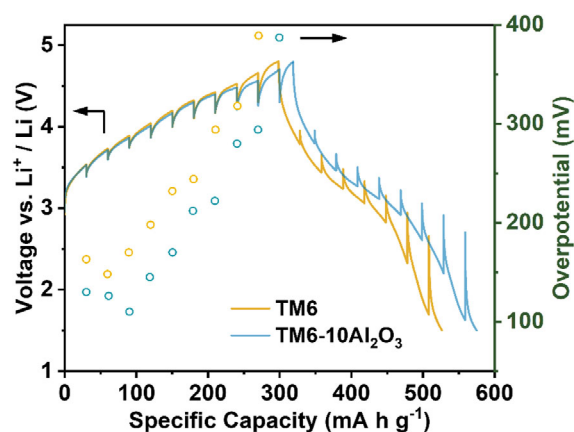


**Figure 6.** GITT curves collected from the TM6 and TM6-10Al<sub>2</sub>O<sub>3</sub> cathodes in the first cycle. The overpotentials at each charging step are shown as dots in the figure.

solid–electrolyte interface film upon cycling.<sup>[44]</sup> Nevertheless, highly oxidized oxygen is likely to aggravate electrolyte decomposition and further impede the lithium diffusion. The reduced resistance after coating also demonstrates that the oxygen-induced side reactions are mitigated by protecting the cathode particle surface. The above results confirm that Al<sub>2</sub>O<sub>3</sub> coating leads to increased interfacial stability, which is consistent with the improved cycling stability and rate performance.

GITT measurements were performed to study the effect of Al<sub>2</sub>O<sub>3</sub> coating on the bulk lithium diffusion kinetics. The GITT method has been primarily used for observing chemical diffusion coefficients from the potential response to a small constant current pulse.<sup>[45]</sup> The GITT curves of TM6 and TM6-10Al<sub>2</sub>O<sub>3</sub> during the first charge and discharge between 1.5 and 4.8 V are shown in **Figure 6**. Less pronounced polarization and reduced overpotential are observed for TM6-10Al<sub>2</sub>O<sub>3</sub>, indicating that Al<sub>2</sub>O<sub>3</sub> coating effectively reduces the bulk lithium diffusion barrier. These results further prove the success of the ALD coating strategy for improving the lithium transport properties and therefore the electrochemical performance of the DRX cathode, which agrees with the above rate performance and EIS results. Overall, electrochemical performance shows that the optimized Al<sub>2</sub>O<sub>3</sub> coating has noteworthy effects on reducing voltage hysteresis, improving reversibility, and increasing ion diffusion of DRX cathode materials.

### 2.3. Gas Analysis

*Operando* DEMS was used to probe the gas evolution of the cathodes with the attempt to investigate the improvement in stability of oxygen redox by this coating strategy. The cells comprising either Al<sub>2</sub>O<sub>3</sub>-coated or uncoated TM6 were cycled in a customized setup in the potential range between 1.5 and 4.8 V at 0.1C rate for two cycles while simultaneously monitoring the gas-gassing behavior. **Figure 7** and Figure S3, Supporting Information, show the DEMS results for the two cathodes.

On the cathode side, O<sub>2</sub> and CO<sub>2</sub> are the most commonly evolved gasses in batteries, both in (Li-rich) layered oxides and DRX materials.<sup>[46,47]</sup> At high state of charge, and especially in

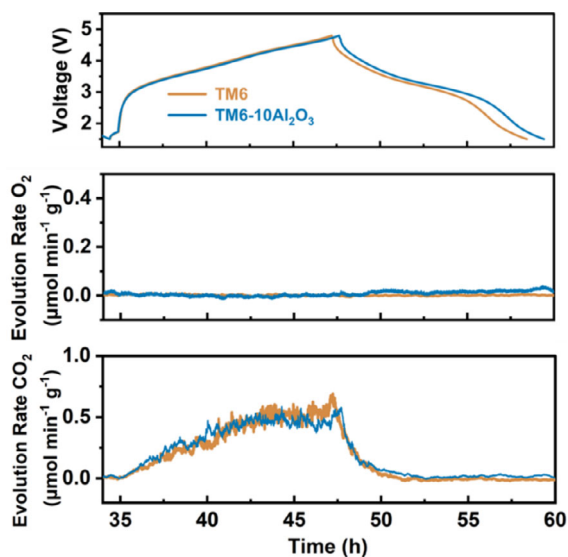


**Figure 7.** Gas evolution of the TM6 and TM6-10Al<sub>2</sub>O<sub>3</sub> cathodes in the second cycle.

Li-rich materials with significant contribution of anionic redox to the overall capacity, lattice oxygen is oxidized and released in the form of highly reactive singlet oxygen <sup>1</sup>O<sub>2</sub>, leaving an oxygen-depleted surface layer of the cathode material behind.<sup>[46,48,49]</sup> Commonly, O<sub>2</sub> gas is not detected directly, or only in traces, as the <sup>1</sup>O<sub>2</sub> reacts with electrolyte, which thus undergoes chemical oxidation under CO<sub>2</sub> evolution.<sup>[50]</sup> However, CO<sub>2</sub> can also be formed by electrochemical oxidation of the electrolyte at potentials above ≈4.7 V versus Li<sup>+</sup>/Li.<sup>[51]</sup> The (chemical<sup>[52]</sup> or electrochemical<sup>[53,54]</sup>) decomposition of Li<sub>2</sub>CO<sub>3</sub> surface impurities further contributes to CO<sub>2</sub> evolution, especially in the first cycle.<sup>[46,55–57]</sup>

Surprisingly, the gas evolution of the materials studied herein is, on the one hand, different from the gassing behavior reported for Li<sub>x</sub>(Co<sub>0.2</sub>Cu<sub>0.2</sub>Mg<sub>0.2</sub>Ni<sub>0.2</sub>Zn<sub>0.2</sub>)OF<sub>x</sub> cathode previously,<sup>[58]</sup> both in curve shape and quantity, and, on the other hand, not distinctively different between coated and uncoated TM6. Especially in the first cycle, both O<sub>2</sub> and CO<sub>2</sub> evolution peak rates are larger by more than one order of magnitude compared to the previous report and also higher than reported for other DRX materials.<sup>[30,59]</sup> In any case, no O<sub>2</sub> evolution was detected in the second cycle, and comparable peak rates for CO<sub>2</sub> evolution were observed. Yet, in this work, the CO<sub>2</sub> evolution in the second cycle is spread out over the whole charge process, instead of in the shape of a peak at the end of charge. The key reason both for the high gas evolution in the first cycle and the broad CO<sub>2</sub> evolution in the second cycle lies in the synthesis procedure. Due to calcination with excess Li and subsequent atmospheric exposure, a large amount of surface Li<sub>2</sub>CO<sub>3</sub> is present, as reported before also for DRX materials.<sup>[56,60,61]</sup> Figure S4, Supporting Information, shows the attenuated total reflection-infrared (ATR-IR) spectra collected from TM6 and TM6-10Al<sub>2</sub>O<sub>3</sub>. The bands located at 1450 and 1500 cm<sup>-1</sup> are antisymmetric stretching vibrations of C-O in Li<sub>2</sub>CO<sub>3</sub>.<sup>[62]</sup> The bands at 866 cm<sup>-1</sup> are assigned to the bending out of plane vibrations of CO<sub>3</sub><sup>2-</sup>.<sup>[63]</sup> These results reveal the presence of residual Li<sub>2</sub>CO<sub>3</sub> on both

samples. After decomposition of most Li<sub>2</sub>CO<sub>3</sub> in the first cycle, crack formation in the electrode continues to expose further surfaces to the electrolyte, explaining the CO<sub>2</sub> evolution in the second cycle.<sup>[44]</sup> In contrast to the behavior observed in the TM6 reported by Lun et al. which only exhibits gas evolution in the first cycle, CO<sub>2</sub> evolution in the second cycle is also observed in this study. This discrepancy might be attributed to a conceptual difference between the DEMS setups employed. DEMS measurement in this work was performed using an open headspace approach, where carrier gas extracts the evolved gasses, while Lun et al. employed a semiclosed headspace, in which the headspace is purged and sampled at regular intervals, resulting in a higher detection limit for CO<sub>2</sub>.<sup>[64]</sup> Furthermore, due to the charge cutoff potential, an electrochemical oxidation of the electrolyte, independent of the cathode material, is likely also contributing to the gas evolution. The reductive degradation at the CEI during the discharging below 2.0 V induces immediate CO<sub>2</sub> evolution upon the start of the subsequent charging.<sup>[65]</sup> Electrochemical oxidation of the surface carbonates may even explain a share of the O<sub>2</sub> evolution observed in the first cycle, as it also involves formation of <sup>1</sup>O<sub>2</sub>.<sup>[53]</sup> A comparison between coated and uncoated material in terms of anionic redox reversibility is complicated by the strong gas evolution from other sources. Especially, a stronger O<sub>2</sub> evolution of the coated material, as shown in Figure S3, Supporting Information, may appear counterintuitive. However, the detection of O<sub>2</sub> implies that the initially formed <sup>1</sup>O<sub>2</sub> was not consumed in further side reactions, but instead relaxed back to ground state <sup>3</sup>O<sub>2</sub>. As the Al<sub>2</sub>O<sub>3</sub> coating is formed around the particles and possible surface impurities are already present after synthesis and ball milling, two possible effects may explain the increased O<sub>2</sub> detection. First, as an acid scavenger coating,<sup>[66]</sup> Al<sub>2</sub>O<sub>3</sub> prevents the chemical decomposition<sup>[52]</sup> of the underlying Li<sub>2</sub>CO<sub>3</sub> by acidic electrolyte degradation products, increasing the share of electrochemical Li<sub>2</sub>CO<sub>3</sub> decomposition under O<sub>2</sub> evolution.<sup>[53,54]</sup> Second, <sup>1</sup>O<sub>2</sub> formed both from carbonate decomposition and from lattice oxygen has to pass through the coating and may during this time already partially relax or be quenched back to <sup>3</sup>O<sub>2</sub>, leading to less follow-up reactions.<sup>[66]</sup> Similar observations have been made in solid-state batteries, where higher O<sub>2</sub> evolution is indicating reduced side reactions both with binder<sup>[67]</sup> and solid electrolyte.<sup>[68]</sup> In conclusion, due to synthesis in Li-excess, gas evolution is dominated by the decomposition of Li<sub>2</sub>CO<sub>3</sub> and analysis thus complicated. A dual role of the Al<sub>2</sub>O<sub>3</sub> coating is proposed that explains the counterintuitively higher O<sub>2</sub> evolution from coated material. First, acid scavenging by the coating leads to Li<sub>2</sub>CO<sub>3</sub> decomposition, not by a chemical, but an electrochemical mechanism involving <sup>1</sup>O<sub>2</sub> evolution. Second, the coating suppresses reactions between evolved <sup>1</sup>O<sub>2</sub> and the electrolyte.

#### 2.4. Interfacial Reactivity

As mentioned above, although the successful Al<sub>2</sub>O<sub>3</sub> coating has been proven to be an effective way to enhance the electrochemical performance of the TM6 cathode, the degradation mechanism during cycling requires further exploration. As recent work has demonstrated, capacity fading in DRX cathodes is caused by the limited lithium transport paths and voltage fading

during the formation of a cation-densified surface.<sup>[69]</sup> In addition, the accumulation of irreversible oxygen loss results in deterioration of the surface layer by direct exposure to the electrolyte.<sup>[70]</sup> The cracks formed in the particles at highly charged states can also lead to severe capacity fading.<sup>[44,71]</sup> To further reveal the effect of coating on the chemical reactions, the surface chemistry and structural changes of the cathodes after cycling were characterized via TEM, XPS, and XRD.

The structural features of the TM6-10Al<sub>2</sub>O<sub>3</sub> cathode after 30 cycles at 0.2C were examined by TEM, as gathered in **Figure 8**. As shown in the indexed SAED pattern, the cathode maintains the rocksalt structure. EDX measurements confirm a uniform distribution of the different elements except for chromium. This can be explained by the migration of Cr<sup>6+</sup> formed in the charged state from octahedral to tetrahedral site.<sup>[72]</sup> After cycling, the Al<sub>2</sub>O<sub>3</sub> coating breaks down partially while maintaining its initial thickness. This result clearly demonstrates that the inert Al<sub>2</sub>O<sub>3</sub> surface coating is only capable of alleviating or delaying the unfavorable reactions with the electrolyte, but it cannot eliminate the irreversible structure deterioration during long-term cycling, which well explains the similar trend in capacity fade rate and rate performance.

XPS detail spectra for the TM6 and TM6-10Al<sub>2</sub>O<sub>3</sub> cathodes after 30 cycles at 0.2C are shown in **Figure 9**. Table S4, Supporting Information, provides the relative atomic concentrations for each species. As shown in the C 1s spectra, an *sp* peak from acetylene black is fitted at an assigned binding energy of 284.0 eV, in agreement with previous publications.<sup>[73–75]</sup> The energy shift of the *sp* carbon peak may be ascribed to differential charging typically occurring on heterogeneous materials with components of differing electrical properties. The partially conductive nature of the samples results in overcompensation of the

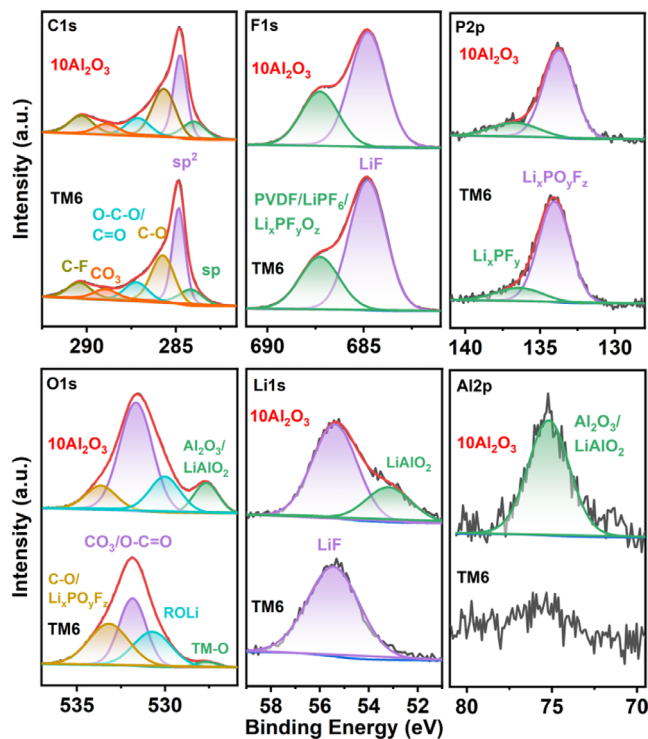


**Figure 9.** XPS data collected from the TM6 and TM6-10Al<sub>2</sub>O<sub>3</sub> cathodes after 30 cycles at 0.2C.

conductive parts, which also makes energy shifts in O 1s explainable.<sup>[76,77]</sup> The peaks characteristic of C–O ( $\approx 285.7$  eV), O–C–O/C=O ( $\approx 287.3$  eV), CO<sub>3</sub> (288.9 eV), and C–F

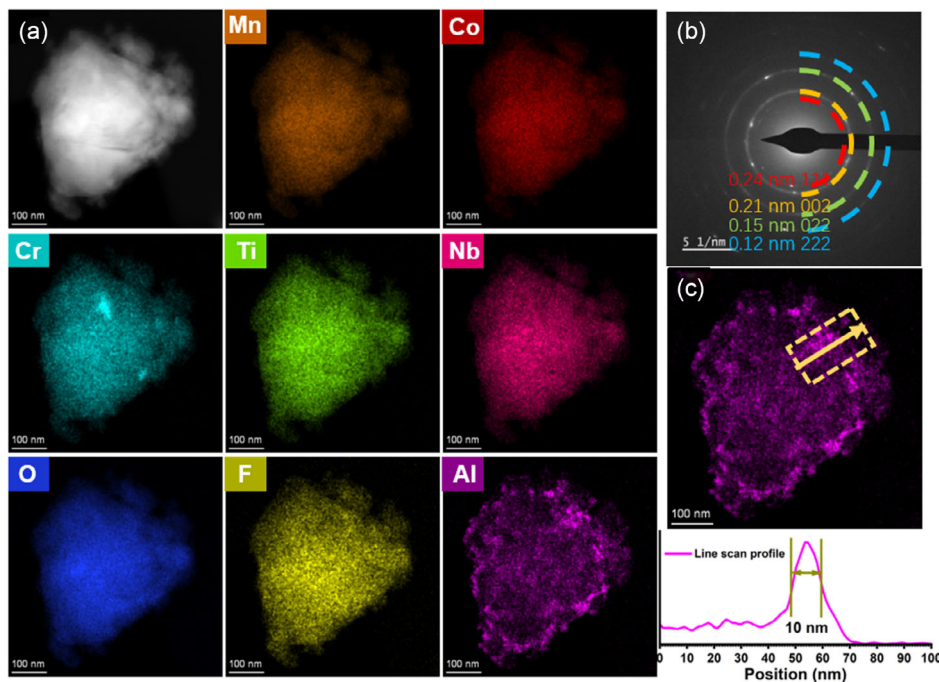


**Figure 8.** a) STEM–EDX mapping and b) SAED pattern of the TM6-10Al<sub>2</sub>O<sub>3</sub> cathode after 30 cycles at 0.2C rate. c) Line scan demonstrating the thickness of the retained coating after cycling. The scale bar in (a), (c) is 100 nm.



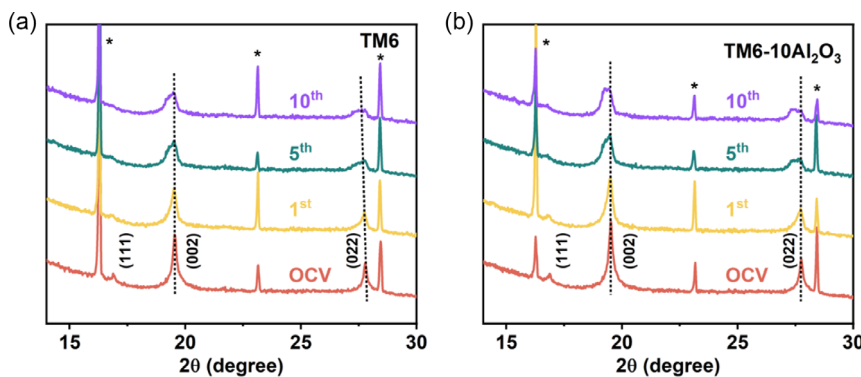


**Figure 10.** XRD patterns of a) TM6 and b) TM6-10Al<sub>2</sub>O<sub>3</sub> cathodes after different cycle numbers (in discharged state). Asterisks denote peaks corresponding to the Li metal.

( $\approx 290.3$  eV) are observed for both cathodes. The total amount of carbon species shows no major differences between the surface chemistry of the TM6 and TM6-10Al<sub>2</sub>O<sub>3</sub> cathodes. The F 1s spectra are composed of two major peaks. The peak at 684.7 eV originates from LiF, which arises from the fluorine in the bulk TM6 and from the degraded electrolyte salt LiPF<sub>6</sub>. The broad peak characteristic of polyvinylidene fluoride (PVDF)(-CF<sub>2</sub>)/LiPF<sub>6</sub>/Li<sub>x</sub>PF<sub>y</sub>O<sub>z</sub> ( $\approx 687.3$  eV) provides evidence for the participation of LiPF<sub>6</sub> salt and fluorinated solvent in surface chemical reactions upon cycling.<sup>[78,79]</sup> This can also be observed from the P 2p spectra with the characteristic binding energies of 134.3 and 136.5 eV.<sup>[80]</sup> For the coated sample, less LiF and LiPF<sub>6</sub>/Li<sub>x</sub>PF<sub>y</sub>O<sub>z</sub> species are observed compared to the uncoated cathode after cycling, indicating a decrease in lithium salt (electrolyte) degradation. For the O 1s spectra, there is a more intense peak around 528 eV for the coated sample, which corresponds to the Al<sub>2</sub>O<sub>3</sub> or LiAlO<sub>2</sub> formed on the surface. After cycling, ROli (alkoxide) ( $\approx 530.7$  eV), surface carbonate or O=C=O ( $\approx 531.9$  eV), and C=O/Li<sub>x</sub>PF<sub>y</sub>O<sub>z</sub> ( $\approx 533.2$  eV) peaks grow for both electrodes, suggesting the decomposition of carbonate solvents.<sup>[81]</sup> The detailed analysis of individual peaks is difficult due to the complicated composition of various oxygen-containing species. For the uncoated sample, these peaks display relatively higher intensities, except for that at  $\approx 531.9$  eV. The large fraction of C=O species for the coated sample might be associated with surface carbonate contamination or esters species stemming from decomposition of the electrolyte solvents.<sup>[82]</sup> Additionally, a more intense peak corresponding to fluorophosphate species, C=O/Li<sub>x</sub>PF<sub>y</sub>O<sub>z</sub> is observed in the uncoated sample, induced by reactions between the cathode surface and HF or PF<sub>6</sub><sup>-</sup>.<sup>[83]</sup> This suggests higher reactivity of electrolyte with the surface of the uncoated sample. In the Li 1s spectra of the coated cathode, a new peak at 53.3 eV is detected, which is identical to the signal of LiAlO<sub>2</sub>, thus suggesting the formation of an ionically conductive LiAlO<sub>2</sub> layer.<sup>[84]</sup> From the Al 2p spectra, aluminum is still clearly visible after cycling, which is consistent with the TEM results. In conclusion, the decrease in the amount of Li-, F-, and P-related species clearly proves that adverse side reactions are alleviated by introducing the Al<sub>2</sub>O<sub>3</sub> coating.

Ex situ XRD measurements were also conducted on the TM6 and TM6-10Al<sub>2</sub>O<sub>3</sub> cathodes after different cycle numbers (1, 5, and 10 cycles) to better understand the structural evolution

upon cycling. As depicted in **Figure 10**, the rocksalt structure of both samples was maintained after several cycles, and the lower peak intensity and broader peak profile suggest reduced crystallinity. In addition, peaks shifts to lower 2-theta degrees indicates an expansion in the rocksalt lattice with cycling.<sup>[85]</sup> After the first cycle, the peak shape becomes less symmetric, suggesting the existence of two rocksalt phases with different lattice parameters. As demonstrated by Chen et al. phase separation occurs during lithium removal from the structure of the Li<sub>1.3-x</sub>Nb<sub>0.3</sub>Mn<sub>0.4</sub>O<sub>2</sub> rocksalt cathode ( $0.4 < x < 1.3$ ).<sup>[71]</sup> Hence, the partially delithiated phase in the discharged state leads to loss of electrochemically accessible Li (gradual vanishing of the 111 diffraction peak for TM6), further leading to capacity decay upon cycling. In the subsequent cycles, the increase in peak splitting suggests a gradual degradation of the DRX structure. The degradation mechanism is possibly associated with significant TM reduction and increased resistivity from the surface to the bulk, making lower amounts of Li<sup>+</sup> accessible and reducing capacity.<sup>[69]</sup> It can also be observed that both coated and uncoated cathodes show a similar phase separation behavior during cycling, and the differences between them are not very pronounced. This explains the analogous trends in capacity fading mentioned previously. These results demonstrate that an ultrathin Al<sub>2</sub>O<sub>3</sub> surface layer is not capable of preventing irreversible structural degradation during battery operation.

### 3. Conclusions

In the present work, ALD-assisted Al<sub>2</sub>O<sub>3</sub> conformal coatings with different thicknesses were deposited onto the surface of high-entropy disordered rocksalt oxyfluoride cathode particles. The ten ALD cycles Al<sub>2</sub>O<sub>3</sub> coating strongly improved the initial specific discharge capacity, rate capability, and cycling stability of the cathode. However, the cells comprising the 20 and 50 ALD cycles Al<sub>2</sub>O<sub>3</sub>-coated cathodes did not show better performance due to the insulating nature of the relatively thick Al<sub>2</sub>O<sub>3</sub> layers. XPS and TEM further proved that the coating strategy can successfully alleviate the side reactions between cathode and electrolyte, with the coating being only partially retained on the cathode after prolonged cycling. Nonetheless, ex situ XRD analysis showed that the ultrathin coating cannot prevent bulk structural

changes from occurring during battery operation. In future studies on the surface modification of DRX cathodes, the phase stability and long-term performance need to be addressed.

## 4. Experimental Section

**Synthesis:** The cathode material  $\text{Li}_{1.3}\text{Mn}^{2+}_{0.1}\text{Co}^{2+}_{0.1}\text{Mn}^{3+}_{0.1}\text{Cr}^{3+}_{0.1}\text{Ti}_{0.1}\text{Nb}_{0.2}\text{O}_{1.7}\text{F}_{0.3}$  (TM6) was synthesized by a typical solid-state method using  $\text{Li}_2\text{CO}_3$  (Sigma–Aldrich, 99.99%),  $\text{MnO}$  (Alfa Aesar, 99%),  $\text{CoCO}_3$  (Alfa Aesar, 99.5%),  $\text{Mn}_2\text{O}_3$  (Sigma–Aldrich, 99%),  $\text{Cr}_2\text{O}_3$  (Alfa Aesar, 98+%),  $\text{TiO}_2$  (Alfa Aesar, 99.5%),  $\text{Nb}_2\text{O}_5$  (Alfa Aesar, 99.5%), and  $\text{LiF}$  (Alfa Aesar, 99.99%) in stoichiometric amounts (except for 10% excess  $\text{Li}_2\text{CO}_3$  and 5% excess  $\text{CoCO}_3$ ). The precursor pellet was heated at 600 °C for 4 h and calcined at 1050 °C for 12 h followed by a quench under Ar atmosphere. The obtained TM6 powder was ball-milled at a rate of 400 rpm for 2 h to reduce the particle size. ALD of  $\text{Al}_2\text{O}_3$  on TM6 powder was performed using TMA (99.99%, Sigma–Aldrich) as Al source and  $\text{H}_2\text{O}$  as the oxygen source at a reactor temperature of 200 °C. Typically, 0.5 g of substrate powder was spread on a gas-permeable sample holder and loaded into the sealed ALD reaction chamber (Picosun). After temperature stabilization for 40 min, vapors of the precursors were alternately purged together with  $\text{N}_2$  gas at a flow rate of 200 sccm into the chamber. A complete ALD cycle includes the following steps: 1) pulsing TMA for 0.5 s; 2) purging the chamber with  $\text{N}_2$  for 45 s; 3) pulsing  $\text{H}_2\text{O}$  for 0.1 s; and 4) purging the chamber with  $\text{N}_2$  for 45 s. The thickness of the  $\text{Al}_2\text{O}_3$  coating was controlled by varying the number of ALD cycles (10, 20, and 50).<sup>[19]</sup> The average growth rate is in the range of 0.1–0.3 nm per cycle.<sup>[20,86,87]</sup> The coated samples are denoted as  $\text{TM6-}n\text{Al}_2\text{O}_3$ , where  $n$  represents the number of ALD cycles. The as-synthesized samples were transferred to an Ar-filled glove box for storage.

**Characterization:** Powder XRD patterns and ex situ patterns of the cathodes after cycling were recorded using a STOE STADI P diffractometer (STOE, Germany) with  $\text{Mo K}\alpha_1$  radiation ( $\lambda = 0.70932 \text{ \AA}$ , 50 kV, 40 mV) and a Mythen2K detector. Refinement of XRD patterns was performed using Fullprof Suite software.

For ex situ XRD, the diffraction data were measured in transmission mode. The cells were terminated at different states of charge (number of cycles) and directly measured without disassembly. Customized CR2032 coin cells with X-ray transparent quartz glass windows (6 mm in diameter, 100  $\mu\text{m}$  thickness) were used for this purpose.<sup>[88]</sup>

SEM measurements were performed on a ZEISS Gemini Leo 1530. TEM measurements were carried out on powder samples dispersed onto a carbon-coated gold grid. The samples were loaded onto a Gatan TEM vacuum transfer holder inside the glove box and transferred to the TEM without exposure to air. SAED and STEM–EDX data were collected using a double-corrected Thermo Fisher Themis-Z equipped with a Super-X EDX detector. The microscope was operated at an accelerating voltage of 300 kV.

XPS measurements were carried out with a Versa Probe III XPS Microprobe (Physical Electronics PHI) equipped with a monochromatic Al  $\text{K}\alpha$  X-ray (1486.6 eV) source. The electrode samples were recovered after cycling by disassembling the coin cells inside the glove box and rinsing them with dimethyl carbonate (DMC). Subsequently, the samples were properly dried under vacuum and transferred to the vacuum chamber of the spectrometer through a transfer chamber. These measures prevent the electrodes from exposure to air and moisture, consistent with conditions described in the literatures.<sup>[80]</sup> XPS data were fitted using XPSPEAK software version 4.1. The binding energies were calibrated using the C 1s peak located at 284.6 eV.

ATR-IR spectra were collected on an ALPHA FT-IR spectrometer (Bruker) equipped with a Ge crystal. The measurements were carried out inside an Ar-filled glove box.

**Electrochemistry:** The active materials were initially ball-milled with Super C65 (Imerys Graphite & Carbon) at 400 rpm for 2 h. The obtained composites were then mixed with 10 wt% acetylene black (Alfa Aesar, 99.9+%) and 10 wt% PVDF (Solef 5130, Solvay) in *N*-methyl-2-pyrrolidone (Alfa Aesar, 99.5%) solution to obtain a slurry using a planetary mixer

(Thinky ARE-250). The active material content in the cathode was 70 wt%. The slurry was coated onto aluminum foil and dried overnight in a vacuum at 120 °C. Afterwards, 13 mm diameter electrodes with an active material loading of 2–3  $\text{mg cm}^{-2}$  were punched out. For the ex situ XRD samples, carbon paper was used as the cathode current collector. For the electrochemical measurements, CR2032-type coin cells were assembled using Li metal foil as anode, GF/D glass microfiber filter paper (Whatman) as separator, and LP30 electrolyte (1M  $\text{LiPF}_6$  in an ethylene carbonate/DMC mixture (1:1 by volume, Sigma–Aldrich)). Half-cells using a Li metal anode were assembled in an Ar-filled glove box ( $\text{O}_2 < 0.1 \text{ ppm}$ ,  $\text{H}_2\text{O} < 0.1 \text{ ppm}$ ) and electrochemically tested on a Land CT2001A battery test system (Wuhan LAND Electronic Co., Ltd) at 25 °C. The galvanostatic cycling tests were carried out at 0.1C rate ( $1\text{C} = 200 \text{ mA g}^{-1}$ ) in a potential range of 1.5–4.8 V versus  $\text{Li}^+/\text{Li}$ . The rate capability tests were performed at C-rates ranging from 0.05 to 2C. CV measurements were performed on a potentiostat (Bio-Logic VSP) at a scan rate of 0.1  $\text{mV s}^{-1}$ . EIS data were recorded using the potentiostat in the frequency range of 1 to 100 MHz with an amplitude of 10 mV. GITT measurements were conducted to analyze the lithium diffusion characteristics in the initial charge/discharge cycle. The GITT pulse duration was 1.5 h at a rate of 0.1C, followed by relaxation of 10 h. The DEMS cell geometry and setup are described in detail elsewhere.<sup>[13,38,74]</sup> The cathode had a diameter of 30 mm with a 4 mm diameter hole in the center allowing the gas flow. During measurement, He was used as a carrier gas and flowed through the cell with the rate of 2.5  $\text{mL min}^{-1}$ . The mass spectrometer was quantitatively calibrated at various partial pressures of  $\text{O}_2$  and  $\text{CO}_2$  in He.

## Supporting Information

Supporting Information is available from the Wiley Online Library or from the author.

## Acknowledgements

B.Z. acknowledges financial support from the China Scholarship Council (CSC). The authors thank Dr. Elmar Y. Kataev (HZB) and Hafssa Arraghraghi (UBT) for helpful discussions on the XPS data. The authors acknowledge the support from the Karlsruhe Nano Micro Facility (KNMFi, www.knmfi.kit.edu), a Helmholtz research infrastructure at Karlsruhe Institute of Technology (KIT, www.kit.edu).

Open Access funding enabled and organized by Projekt DEAL. Funded by the Open Access Publishing Fund of the University of Bayreuth.

## Conflict of Interest

The authors declare no conflict of interest.

## Data Availability Statement

The data that support the findings of this study are available from the corresponding author upon reasonable request.

## Keywords

atomic layer deposition, cathode–electrolyte interface, disordered rocksalt, lithium-ion batteries

Received: January 7, 2024

Revised: March 21, 2024

Published online: April 7, 2024

- [1] R. Wang, X. Li, L. Liu, J. Lee, D.-H. Seo, S.-H. Bo, A. Urban, G. Ceder, *Electrochem. Commun.* **2015**, *60*, 70.
- [2] Z. Lu, L. Y. Beaulieu, R. A. Donaberger, C. L. Thomas, J. R. Dahn, *J. Electrochem. Soc.* **2002**, *149*, A778.
- [3] J. Lee, D. H. Seo, M. Balasubramanian, N. Twu, X. Li, G. Ceder, *Energy Environ. Sci.* **2015**, *8*, 3255.
- [4] R. Wang, X. He, L. He, F. Wang, R. Xiao, L. Gu, H. Li, L. Chen, *Adv. Energy Mater.* **2013**, *3*, 1358.
- [5] J. Lee, A. Urban, X. Li, D. Su, G. Hautier, G. Ceder, *Science* **2014**, *343*, 519.
- [6] M. J. Crafton, Y. Yue, T. Huang, W. Tong, B. D. McCloskey, *Adv. Energy Mater.* **2020**, *10*, 2001500.
- [7] M. M. Rahman, F. Lin, *Matter* **2021**, *4*, 490.
- [8] D.-H. Seo, J. Lee, A. Urban, R. Malik, S. Kang, G. Ceder, *Nat. Chem.* **2016**, *8*, 692.
- [9] Z. Lun, B. Ouyang, D.-H. Kwon, Y. Ha, E. E. Foley, T.-Y. Huang, Z. Cai, H. Kim, M. Balasubramanian, Y. Sun, J. Huang, Y. Tian, H. Kim, B. D. McCloskey, W. Yang, R. J. Clément, H. Ji, G. Ceder, *Nat. Mater.* **2021**, *20*, 214.
- [10] Q. Wang, A. Sarkar, D. Wang, L. Velasco, R. Azmi, S. S. Bhattacharya, T. Bergfeldt, A. Düvel, P. Heitjans, T. Brezesinski, H. Hahn, B. Breitung, *Energy Environ. Sci.* **2019**, *12*, 2433.
- [11] J. Song, F. Ning, Y. Zuo, A. Li, H. Wang, K. Zhang, T. Yang, Y. Yang, C. Gao, W. Xiao, Z. Jiang, T. Chen, G. Feng, D. Xia, *Adv. Mater.* **2023**, *35*, 2208726.
- [12] K. McColl, R. A. House, G. J. Rees, A. G. Squires, S. W. Coles, P. G. Bruce, B. J. Morgan, M. S. Islam, *Nat. Commun.* **2022**, *13*, 5275.
- [13] B. Breitung, Q. Wang, A. Schiele, Đ. Tripković, A. Sarkar, L. Velasco, D. Wang, S. S. Bhattacharya, H. Hahn, T. Brezesinski, *Batteries Supercaps* **2020**, *3*, 361.
- [14] J. L. Tebbe, A. M. Holder, C. B. Musgrave, *ACS Appl. Mater. Interfaces* **2015**, *7*, 24265.
- [15] H. Liu, D. Qian, M. G. Verde, M. Zhang, K. J. Carroll, D. Lau, M. Chi, G. M. Veith, Y. S. Meng, *ACS Appl. Mater. Interfaces* **2015**, *9*, 19189.
- [16] J. Kang, B. Han, *ACS Appl. Mater. Interfaces* **2015**, *7*, 11599.
- [17] R. A. House, J. J. Marie, M. A. Pérez-Osorio, G. J. Rees, E. Boivin, P. G. Bruce, *Nat. Energy* **2021**, *6*, 781.
- [18] W. Guo, C. Zhang, Y. Zhang, L. Lin, W. He, Q. Xie, B. Sa, L. Wang, D. Peng, *Adv. Mater.* **2021**, *33*, 2103173.
- [19] D. Kitsche, Y. Tang, H. Hemmelmann, F. Walther, M. Bianchini, A. Kondrakov, J. Janek, T. Brezesinski, *Small Sci.* **2023**, *3*, 2200073.
- [20] D. Kitsche, Y. Tang, Y. Ma, D. Goonetilleke, J. Sann, F. Walther, M. Bianchini, J. Janek, T. Brezesinski, *ACS Appl. Energy Mater.* **2021**, *4*, 7338.
- [21] D. Guan, J. A. Jeevarajan, Y. Wang, *Nanoscale* **2011**, *3*, 1465.
- [22] B. Huang, R. Wang, Y. Gong, B. He, H. Wang, *Front. Chem.* **2019**, *7*, 107.
- [23] A. M. Wise, C. Ban, J. N. Weker, S. Misra, A. S. Cavanagh, Z. Wu, Z. Li, M. S. Whittingham, K. Xu, S. M. George, M. F. Toney, *Chem. Mater.* **2015**, *27*, 6146.
- [24] B. Xiao, B. Wang, J. Liu, K. Kaliyappan, Q. Sun, Y. Liu, G. Dadheech, M. P. Balogh, L. Yang, T.-K. Sham, R. Li, M. Cai, X. Sun, *Nano Energy* **2017**, *34*, 120.
- [25] B. Han, B. Key, A. S. Lipton, J. T. Vaughey, B. Hughes, J. Trevey, F. Dogan, *J. Electrochem. Soc.* **2019**, *166*, A3679.
- [26] W. Zhu, X. Huang, T. Liu, Z. Xie, Y. Wang, K. Tian, L. Bu, H. Wang, L. Gao, J. Zhao, *Coatings* **2019**, *9*, 92.
- [27] H. Zhang, J. Xu, J. Zhang, *Front. Mater.* **2019**, *6*, 309.
- [28] X. Zhang, I. Belharouak, L. Li, Y. Lei, J. W. Elam, A. Nie, X. Chen, R. S. Yassar, R. L. Axelbaum, *Adv. Energy Mater.* **2013**, *3*, 1299.
- [29] B. Wu, Y. Ren, D. Mu, X. Liu, G. Yang, F. Wu, *RSC Adv.* **2014**, *4*, 10196.
- [30] Z. Lun, B. Ouyang, D.-H. Kwon, Y. Ha, E. E. Foley, T.-Y. Huang, Z. Cai, H. Kim, M. Balasubramanian, Y. Sun, J. Huang, Y. Tian, H. Kim, B. D. McCloskey, W. Yang, R. J. Clément, H. Ji, G. Ceder, *Nat. Mater.* **2021**, *20*, 214.
- [31] T. Huang, Z. Cai, M. J. Crafton, L. A. Kaufman, Z. M. Konz, H. K. Bergstrom, E. A. Kedzie, H. Hao, G. Ceder, B. D. McCloskey, *Adv. Energy Mater.* **2023**, *13*, 2300241.
- [32] T.-Y. Huang, M. J. Crafton, Y. Yue, W. Tong, B. D. McCloskey, *Energy Environ. Sci.* **2021**, *14*, 1553.
- [33] R. Chen, C. L. A. Leung, C. Huang, *Adv. Funct. Mater.* **2024**, 2308165.
- [34] I. Källquist, A. J. Naylor, C. Baur, J. Chable, J. Kullgren, M. Fichtner, K. Edström, D. Brandell, M. Hahlin, *Chem. Mater.* **2019**, *31*, 6084.
- [35] D. Chen, J. Wu, J. K. Papp, B. D. McCloskey, W. Yang, G. Chen, *Small* **2020**, *16*, 2000656.
- [36] Z. Lun, B. Ouyang, Z. Cai, R. J. Clément, D.-H. Kwon, J. Huang, J. K. Papp, M. Balasubramanian, Y. Tian, B. D. McCloskey, H. Ji, H. Kim, D. A. Kitchaev, G. Ceder, *Chem* **2020**, *6*, 153.
- [37] F. Geng, B. Hu, C. Li, C. Zhao, O. Lafon, J. Trébosc, J.-P. Amoureux, M. Shen, B. Hu, *J. Mater. Chem. A* **2020**, *8*, 16515.
- [38] J. Huang, J. Zhang, *J. Electrochem. Soc.* **2016**, *163*, A1983.
- [39] Y. Zhang, Z. Liu, Z. Wang, Y. Jiang, G. Wen, P. Gao, Y. Zhu, *Electrochim. Acta* **2019**, *310*, 136.
- [40] X.-Y. Qiu, Q.-C. Zhuang, Q.-Q. Zhang, R. Cao, P.-Z. Ying, Y.-H. Qiang, S.-G. Sun, *Phys. Chem. Chem. Phys.* **2012**, *14*, 2617.
- [41] J. Liu, B. Reeja-Jayan, A. Manthiram, *J. Phys. Chem. C* **2010**, *114*, 9528.
- [42] A. Garcia, G. Torres-Treviño, A. R. West, *Solid State Ionics* **1990**, *40–41*, 13.
- [43] M. J. Herzog, N. Gauquelin, D. Esken, J. Verbeeck, J. Janek, *Energy Technol.* **2021**, *9*, 2100028.
- [44] S. Schweidler, S. L. Dreyer, B. Breitung, T. Brezesinski, *Coatings* **2022**, *12*, 402.
- [45] E. Deiss, *Electrochim. Acta* **2005**, *50*, 2927.
- [46] S. L. Dreyer, A. Kondrakov, J. Janek, T. Brezesinski, *J. Mater. Res.* **2022**, *37*, 3146.
- [47] P. Liu, L. Yang, B. Xiao, H. Wang, L. Li, S. Ye, Y. Li, X. Ren, X. Ouyang, J. Hu, F. Pan, Q. Zhang, J. Liu, *Adv. Funct. Mater.* **2022**, *32*, 2208586.
- [48] J. Wandt, A. T. S. Freiberg, A. Ogrodnik, H. A. Gasteiger, *Mater. Today* **2018**, *21*, 825.
- [49] D. Streich, C. Erk, A. Guéguen, P. Müller, F.-F. Chesneau, E. J. Berg, *J. Phys. Chem. C* **2017**, *121*, 13481.
- [50] R. Jung, M. Metzger, F. Maglia, C. Stinner, H. A. Gasteiger, *J. Phys. Chem. Lett.* **2017**, *8*, 4820.
- [51] M. Metzger, P. Walke, S. Solchenbach, G. Salitra, D. Aurbach, H. A. Gasteiger, *J. Electrochem. Soc.* **2020**, *167*, 160522.
- [52] A. T. S. Freiberg, J. Sicklinger, S. Solchenbach, H. A. Gasteiger, *Electrochim. Acta* **2020**, *346*, 136271.
- [53] N. Mahne, S. E. Renfrew, B. D. McCloskey, S. A. Freunberger, *Angew. Chem. Int. Ed.* **2018**, *57*, 5529.
- [54] L. A. Kaufman, B. D. McCloskey, *Chem. Mater.* **2021**, *33*, 4170.
- [55] T. Hatsukade, A. Schiele, P. Hartmann, T. Brezesinski, J. Janek, *ACS Appl. Mater. Interfaces* **2018**, *10*, 38892.
- [56] S. E. Renfrew, B. D. McCloskey, *J. Am. Chem. Soc.* **2017**, *139*, 17853.
- [57] F. Strauss, J. H. Teo, A. Schiele, T. Bartsch, T. Hatsukade, P. Hartmann, J. Janek, T. Brezesinski, *ACS Appl. Mater. Interfaces* **2020**, *12*, 20462.
- [58] B. Breitung, Q. Wang, A. Schiele, Đ. Tripković, A. Sarkar, L. Velasco, D. Wang, S. S. Bhattacharya, H. Hahn, T. Brezesinski, *Batteries Supercaps* **2020**, *3*, 361.
- [59] Z. Lun, B. Ouyang, D. A. Kitchaev, R. J. Clément, J. K. Papp, M. Balasubramanian, Y. Tian, T. Lei, T. Shi, B. D. McCloskey, J. Lee, G. Ceder, *Adv. Energy Mater.* **2019**, *9*, 1802959.
- [60] J. Lee, D. A. Kitchaev, D.-H. Kwon, C.-W. Lee, J. K. Papp, Y.-S. Liu, Z. Lun, R. J. Clément, T. Shi, B. D. McCloskey, J. Guo, M. Balasubramanian, G. Ceder, *Nature* **2018**, *556*, 185.
- [61] W. M. Seong, Y. Kim, A. Manthiram, *Chem. Mater.* **2020**, *32*, 9479.

- [62] W. Cai, R. Chen, Y. Yang, M. Yi, L. Xiang, *Crystals* **2018**, *8*, 19.
- [63] P. Pasierb, S. Komornicki, M. Rokita, M. Rękas, *J. Mol. Struct.* **2001**, *596*, 151.
- [64] S. L. Dreyer, A. Kondrakov, J. Janek, T. Brezesinski, *J. Mater. Res.* **2022**, *37*, 3146.
- [65] M. J. Crafton, T.-Y. Huang, Z. Cai, Z. M. Konz, N. Guo, W. Tong, G. Ceder, B. D. McCloskey, *J. Electrochem. Soc.* **2024**, *171*, 020530.
- [66] S. L. Dreyer, K. R. Kretschmer, Đ. Tripković, A. Mazilkin, R. Chukwu, R. Azmi, P. Hartmann, M. Bianchini, T. Brezesinski, J. Janek, *Adv. Mater. Interfaces* **2022**, *9*, 2101100.
- [67] J. H. Teo, F. Strauss, D. Tripković, S. Schweidler, Y. Ma, M. Bianchini, J. Janek, T. Brezesinski, *Cell Rep. Phys. Sci.* **2021**, *2*, 100465.
- [68] J. H. Teo, F. Strauss, F. Walther, Y. Ma, S. Payandeh, T. Scherer, M. Bianchini, J. Janek, T. Brezesinski, *Mater. Futures* **2022**, *1*, 015102.
- [69] D. Chen, W. H. Kan, G. Chen, *Adv. Energy Mater.* **2019**, *9*, 1901255.
- [70] L. Li, Z. Lun, D. Chen, Y. Yue, W. Tong, G. Chen, G. Ceder, C. Wang, *Adv. Funct. Mater.* **2021**, *31*, 2101888.
- [71] W. H. Kan, D. Chen, J. K. Papp, A. K. Shukla, A. Huq, C. M. Brown, B. D. McCloskey, G. Chen, *Chem. Mater.* **2018**, *30*, 1655.
- [72] J. Huang, P. Zhong, Y. Ha, D.-H. Kwon, M. J. Crafton, Y. Tian, M. Balasubramanian, B. D. McCloskey, W. Yang, G. Ceder, *Nat. Energy* **2021**, *6*, 706.
- [73] M. Rybachuk, J. M. Bell, *Carbon* **2009**, *47*, 2481.
- [74] L. Zhang, H. Ma, N. Yao, Z. Lu, B. Zhang, *J. Vac. Sci. Technol., B* **2007**, *25*, 545.
- [75] A. Hu, S. Griesing, M. Rybachuk, Q.-B. Lu, W. W. Duley, *J. Appl. Phys.* **2007**, *102*, 074311.
- [76] T. L. Barr, *J. Vac. Sci. Technol., A* **1989**, *7*, 1677.
- [77] J. M. Gorham, W. A. Osborn, J. W. Woodcock, K. C. K. Scott, J. M. Heddleston, A. R. Hight Walker, J. W. Gilman, *Carbon* **2016**, *96*, 1208.
- [78] Q. Li, Y. Wang, X. Wang, X. Sun, J.-N. Zhang, X. Yu, H. Li, *ACS Appl. Mater. Interfaces* **2020**, *12*, 2319.
- [79] N. Schulz, R. Hausbrand, C. Wittich, L. Dimesso, W. Jaegermann, *J. Electrochem. Soc.* **2018**, *165*, A833.
- [80] S. Verdier, L. E. Ouatani, R. Dedryvère, F. Bonhomme, P. Biensan, D. Gonbeau, *J. Electrochem. Soc.* **2007**, *154*, A1088.
- [81] S. Watanabe, M. Kinoshita, T. Hosokawa, K. Morigaki, K. Nakura, *J. Power Sources* **2014**, *258*, 210.
- [82] J. Alvarado, C. Ma, S. Wang, K. Nguyen, M. Kodur, Y. S. Meng, *ACS Appl. Mater. Interfaces* **2017**, *9*, 26518.
- [83] N. D. Phillip, C. Daniel, G. M. Veith, *J. Electrochem. Soc.* **2020**, *167*, 040521.
- [84] X. Li, J. Liu, B. Wang, M. N. Banis, B. Xiao, R. Li, T.-K. Sham, X. Sun, *RSC Adv.* **2014**, *4*, 27126.
- [85] S. Zheng, D. Liu, L. Tao, X. Fan, K. Liu, G. Liang, A. Dou, M. Su, Y. Liu, D. Chu, *J. Alloys Compd.* **2019**, *773*, 1.
- [86] Y. Shi, M. Zhang, D. Qian, Y. S. Meng, *Electrochim. Acta* **2016**, *203*, 154.
- [87] J. W. Kim, D. H. Kim, D. Y. Oh, H. Lee, J. H. Kim, J. H. Lee, Y. S. Jung, *J. Power Sources* **2015**, *274*, 1254.
- [88] M. Akhtar, H. Arraghraghi, S. Kunz, Q. Wang, M. Bianchini, *J. Mater. Chem. A* **2023**, *11*, 25650.